



# CHORUS

This is the accepted manuscript made available via CHORUS. The article has been published as:

## In situ Investigation of Magnetism in Metastable Phases of Levitated Fe<sub>{83}</sub>B<sub>{17}</sub> During Solidification

D. G. Quirinale, D. Messina, G. E. Rustan, A. Kreyssig, R. Prozorov, and A. I. Goldman  
Phys. Rev. Applied **8**, 054046 — Published 22 November 2017

DOI: [10.1103/PhysRevApplied.8.054046](https://doi.org/10.1103/PhysRevApplied.8.054046)

# *In-situ* investigation of magnetism in metastable phases in levitated Fe<sub>83</sub>B<sub>17</sub>

D. G. Quirinale,<sup>1</sup> D. Messina,<sup>1</sup> G. E. Rustan,<sup>1</sup> A. Kreyssig,<sup>1,2</sup> R. Prozorov,<sup>1,2</sup> and A. I. Goldman<sup>1,2</sup>

<sup>1</sup>*Department of Physics and Astronomy, Iowa State University, Ames, Iowa 50011, USA*

<sup>2</sup>*Ames Laboratory, USDOE, Iowa State University, Ames, Iowa 50011, USA*

(Dated: October 9, 2017)

*In-situ* measurements of structure, density, and magnetization on samples of Fe<sub>83</sub>B<sub>17</sub> using an electrostatic levitation furnace have allowed us to identify and correlate the magnetic and structural transitions in this system during its complex solidification process. In particular, we have identified magnetic ordering in the metastable Fe<sub>23</sub>B<sub>6</sub>/*fcc*-Fe coherently grown structures and primitive tetragonal-Fe<sub>3</sub>B metastable phase in addition to characterizing the equilibrium Fe<sub>2</sub>B phase. Our measurements demonstrate that the incorporation of a tunnel-diode oscillator circuit within an electrostatic levitation furnace enables new investigations of the physical properties of high-temperature metastable structures.

## I. INTRODUCTION

Thermophysical properties such as density, specific heat, viscosity, surface tension, emissivity, conductivity and magnetization provide valuable insight into the nature of the metastable solids and liquids, and critical data for quantitative modeling of phase selection and solidification. However, metastable phases at high temperature are notoriously difficult to characterize, particularly when environmental contamination is of concern. Nevertheless, the ability to determine *in-situ* both the structure and properties of these metastable phases, their formation with composition and temperature, and their role in the formation or inhibition of stable phases at lower temperatures can add tremendously to our understanding of stable phase formation in complex systems.

The Fe-B binary system has been the subject of intense study for decades since it is a constituent of magnetic materials critical to a number of industries[1–3] as well as the essential component of a number of metallic glasses[4, 5]. Devitrification experiments on glassy samples have observed an abundance of metastable phases, such as primitive tetragonal (*pt*) Fe<sub>3</sub>B, body-centered tetragonal (*bct*) Fe<sub>3</sub>B, orthorhombic (*o*) Fe<sub>3</sub>B, and cubic Fe<sub>23</sub>B<sub>6</sub>. *In-situ* studies [6–8] have provided additional insights into the solidification pathways in eutectic Fe<sub>83</sub>B<sub>17</sub>. In particular our recent *in-situ* high-energy x-ray studies[9, 10] of Fe<sub>83</sub>B<sub>17</sub> have revealed that this alloy solidifies either directly into the equilibrium Fe<sub>2</sub>B + *fcc*-Fe phases, or a metastable phase mixture of Fe<sub>23</sub>B<sub>6</sub> + *fcc*-Fe that, subsequently, either transforms to the equilibrium high-temperature phases (Fe<sub>2</sub>B + *fcc*-Fe) or persists down to ambient temperature. The same sample, undergoing the same heating process and free-cooling, exhibits both solidification behaviours in sequence, with no discernible difference in cooling rates between the different pathways[9, 10]. The sequence of solidification products for samples where the metastable Fe<sub>23</sub>B<sub>6</sub> phase persists to ambient temperature is quite complex. For example, the Fe<sub>83</sub>B<sub>17</sub> phase is accompanied by the presence of coherently grown *fcc*-Fe which also persists to temperatures well below the allotropic *fcc* - *bcc* transition at

~1150 K on cooling, and the metastable *pt*-Fe<sub>3</sub>B is also observed at lower temperatures.

Given the past emphasis on the magnetic properties of the Fe<sub>23</sub>B<sub>6</sub> phase[11], as well as extensive investigations into the magnetism of *fcc* Fe structures stabilized on a variety of substrates[12–14], there is considerable interest in the nature and formation of magnetism in these non-equilibrium phases. The complex nature of the solidification, however, requires a probe that is well suited to the challenges of high temperature, the time dependence of the solidification process itself, and the requisite sensitivity to detect the subtle signals of the emergent magnetism. To overcome these challenges, the containerless environment of an electrostatic levitation furnace has been combined with a tunnel-diode oscillating (TDO) circuit adapted for high temperature processing, enabling precision contactless measurements of dynamic magnetic susceptibility[15, 16]. While the TDO method has traditionally been employed as a highly sensitive probe of resistivity, susceptibility, and London penetration depth in the low temperature regime, here it has been adapted for use in high temperature processing.

Applied concurrently with simultaneous volumetric measurements, and correlated with high-energy x-ray diffraction experiments for phase determination, we have identified and characterized a number of magnetic transitions during the solidification of Fe<sub>83</sub>B<sub>17</sub>. Several new results, including an enhanced magnetic ordering temperature for Fe<sub>23</sub>B<sub>6</sub>, are obtained from our measurements.

## II. EXPERIMENTAL DETAILS

### A. Sample Preparation

Fe<sub>83</sub>B<sub>17</sub> ingots were prepared by arc melting 99.99% pure Fe from Toho Zinc Corporation and 99.9999% pure B from Alfa Aesar. A reducing atmosphere was used inside the arc melter to prevent oxidation and facilitate the dissolution of oxide phases in the source material. The produced ingots were then broken into small chunks ranging in size from 30 to 80 mg. These pieces were

placed on a polished graphite surface and laser melted several times to form the spheres desired for stable levitation. The first melt was performed under an Airgas forming gas (5% H<sub>2</sub>, 95% Ar<sub>2</sub>), and the sample, now a molten sphere, was held in the liquid state until the surface was visibly clear of oxide patches. The samples were subsequently briefly melted in a high vacuum ( $\sim 10^{-7}$  torr) to assist in pre-levitation degassing. All material was carefully massed before and after each processing step to control evaporative mass-loss and the associated stoichiometry shift. In addition, a Leco CS-444 carbon determinator was used to measure potential carbon contamination from the graphite substrates. No appreciable difference in carbon content was found between the raw material and the graphite-processed spheres.

### B. Electrostatic Levitation

The samples were levitated in the ISU-ESL, which has been described in detail elsewhere [15, 16]. The positioning system was based on a pair of orthogonal LEDs casting shadows of the sample on position-sensitive detectors (PSDs). Combined with a high speed feedback loop operating at 500 Hz, the sample position could be maintained to within 3-5  $\mu$ [15]. Bi-directional sample heating was accomplished using a fiber-coupled laser. Controlled heating and cooling ramps were performed using a PID algorithm in the LabVIEW laser control program at a rate of 2 K/s. All samples were freely cooled through the initial solidification plateau by turning off the laser, with any cooling rates applied once solidification had completed, in order to not bias the phase selection process. The data presented here were taken on a 43 mg sample, exhibiting  $\sim 0.1$  mg of mass loss through the course of 10 heating and cooling cycles. Volumetric measurements were performed in the ISU-ESL using a well established videographic algorithm [16, 18, 19] and were performed concurrently with the TDO measurements to ensure that the observed magnetic transitions could be correlated consistently with transitions in the x-ray data.

### C. Tunnel Diode Oscillator

The ISU-ESL TDO is described in detail in Refs. 15 and 16. Briefly, a copper coil was installed in the bottom electrode of the ESL and connected to a tank circuit driven by a tunnel diode biased to the region of negative differential resistance on its  $V(I)$  curve. Samples levitating above the coil are inductively coupled to coil (inductor) of the oscillator circuit and changes in the sample conductivity and/or magnetization result in a shift of the circuit's resonant frequency  $f_0 = (2\pi\sqrt{LC})^{-1}$ :

$$\frac{\Delta f}{f_0} = \frac{3}{4}\phi\left(1 - \frac{3\delta}{2a}(1 + \chi)\right) \quad (1)$$

where  $\Delta f$  is the shift in frequency,  $f_0$  is the resonant frequency of the empty circuit without the sample,  $\phi$  is the sample filling factor, and  $\chi = \mu - 1$  is the magnetic susceptibility. In general, the frequency shift is proportional to the total magnetic susceptibility of the sample, which consists of both skin - effect diamagnetism and electronic magnetism - either dia- or para- depending on the situation. The latter contributes from the skin depth layer accessible to the AC excitation field. As we show below, the onset of magnetic ordering can produce frequency shifts of  $10^2$ - $10^3$  Hz. Any effects of temperature fluctuations of the coil itself are mitigated using the procedure for background subtraction outlined in Ref. 15.

### D. High-energy X-ray Diffraction

High-energy x-ray diffraction measurements were performed at Beamline 6-ID-D ( $\lambda = 0.09411$  Å,  $E = 131$  keV) at the Advanced Photon Source (APS) at Argonne National Laboratory. The samples were levitated in the Washington University Beamline Electrostatic Levitator (WU-BESL), a detailed description of which can be found in Ref. 20, and processed using a similar procedure to the one described in Ref. 10. A two-dimensional GE Revolution 41-RT amorphous silicon flat-panel detector was used for rapid acquisition of diffraction patterns in transmission geometry, with  $\sim 88\%$  transmission through the sample. All x-ray data presented here were obtained at 1 frame per second on a single 46 mg sample. Diffraction patterns were obtained on both cooling and heating, so that phases present could be thoroughly established and correlated with the TDO measurements. No automated temperature control was available but efforts were made to match the ramp rates used for the TDO study. Gaps in the x-ray data are due to detector memory limits on continuous acquisitions. ImageJ[21] was used to correct diffraction images for dark current and background. Fit2D[22, 23] was used to determine detector distance, correct for detector rotation and tilt, and azimuthally integrate the 2D data. GSAS[24] was used for all sequential Rietveld refinements.

## III. RESULTS

### A. Equilibrium Solidification

In Fig. 1 we show the x-ray, volumetric and TDO data for a cooling/heating cycle where the Fe<sub>83</sub>B<sub>17</sub> sample solidifies into the equilibrium Fe<sub>2</sub>B + *fcc*-Fe phases from the melt. Here, the cooling rate was controlled by applying the laser starting 100 K below the solidification plateau, after initial phase selection had occurred. Fe<sub>2</sub>B is the primary equilibrium phase, accompanied by *fcc*-Fe at high temperature which transforms to *bcc*-Fe near  $T = 1150$  K. The transformation of *fcc*-Fe to *bcc*-Fe represents a shift in average volume per Fe atom from 12.188

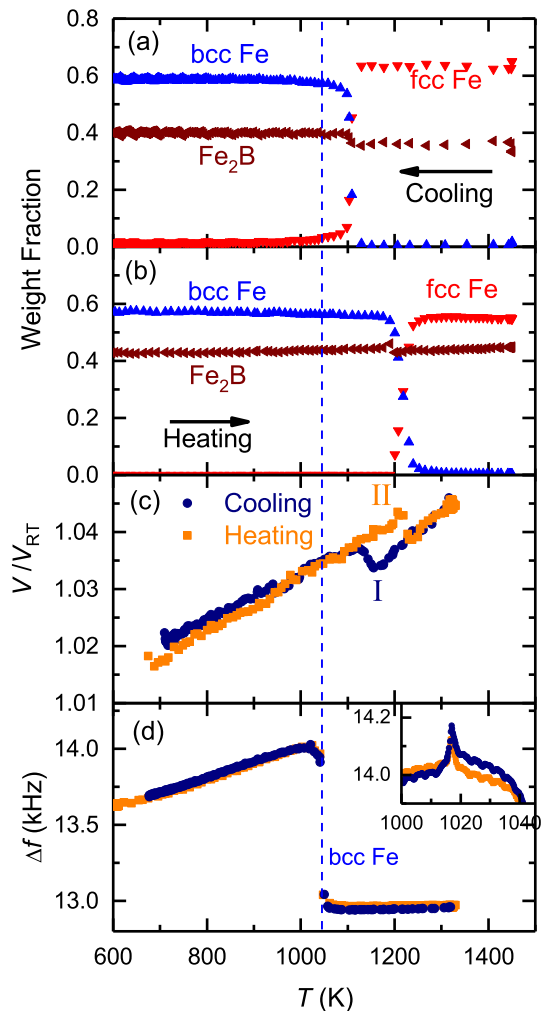


FIG. 1. (color online) (a) and (b) Results of Rietveld refinements of the x-ray data. The red triangles represent *fcc*-Fe, blue triangles represent *bcc*-Fe, and the brown triangles represent  $\text{Fe}_2\text{B}$ . Weight fractions in panel (a) were measured on cooling, and those in (b) were measured on heating. (c) Volumetric data taken in the ISU-ESL, represented as fractional changes from ambient temperature values. Temperatures labeled as I and II denote the allotropic transition on cooling and heating, respectively. (d) Frequency shift measured by the TDO circuit. The inset displays the peak near 1018 K taken on a similarly-sized sample with data taken at a lower cooling and heating rate ( $\sim 0.25$  K/s) for higher resolution. Dark blue circles correspond to cooling and orange squares represent the subsequent reheat.

$\text{\AA}^3/\text{atom}$  to  $12.238 \text{ \AA}^3/\text{atom}$ , which is reflected in the cooling curve in Fig. 1(c) as an expansion at the transition. On heating, the *bcc*-Fe to *fcc*-Fe transition is observed in the x-ray data at 1220 K, and the corresponding volume contraction is seen in Fig. 1(c) at nearly the same temperature.

The TDO data in Fig. 1(d) exhibits a sizeable frequency shift (proportional to the magnetic susceptibility of the sample) at 1040 K, with a magnitude of 1080

Hz, signifying a large increase in magnetic susceptibility corresponding to the onset of magnetic ordering. This temperature closely matches the known Curie temperature ( $T_C$ ) for the onset of ferromagnetism for *bcc*-Fe of 1043 K. On heating, a comparable decrease in frequency is observed at the same temperature, signaling the transition from ferromagnetic order below, to paramagnetism above,  $T_C$ . Furthermore, there is a small but persistent peak at 1018 K. The well-established  $T_C$  for  $\text{Fe}_2\text{B}$  of 1015 K[25] suggests this feature arises from the ferromagnetic ordering of  $\text{Fe}_2\text{B}$ . Both the shape and the magnitude of this feature, however, are quite different from the step-like TDO frequency shift observed for the ferromagnetic ordering of *bcc*-Fe.

Extensive investigations into the TDO response to magnetic transitions have determined that large, step-like increases in the frequency shift are associated with the onset of itinerant ferromagnetism[26], consistent with the itinerant magnetism in *bcc*-Fe. Alternatively, ferromagnetic transitions in local moment systems demonstrate small, sharp peaks in the frequency shift[26, 27] due to critical fluctuations. The shape and small frequency shift of the  $\text{Fe}_2\text{B}$  transition with respect to its weight fraction is consistent with past evidence for local moment magnetism in  $\text{Fe}_2\text{B}$ [28]. These results further demonstrate that the nature of the ordering (local vs. itinerant) in magnetic materials, as well as the ordering temperature itself, may be elucidated through TDO measurements.

## B. Metastable Solidification

We now turn to our measurements, displayed in Fig. 2, for a cooling/heating cycle where the  $\text{Fe}_{83}\text{B}_{17}$  sample solidifies into the metastable  $\text{Fe}_{23}\text{B}_6 + \text{fcc}$ -Fe phases from the melt. This cycle was performed subsequent to the cycle presented in Fig. 1, on the same sample. To ensure the capture of the kinetics of the metastable phase transitions with temperature, all of these data were taken while free-cooling the sample from high temperature, as applying the laser to control the cooling rate after solidification often resulted in a metastable to equilibrium transformation. Fig. 2(a) and (b) are again the calculated weight fractions from the Rietveld refinements of the x-ray data during cooling and heating, respectively, and are consistent with our previous results[9, 10].

On cooling, the *fcc*-Fe to *bcc*-Fe transformation is suppressed to much lower temperature, commencing at approximately 1050 K, and is quite broad in temperature. A small weight fraction of the metastable *pt*- $\text{Fe}_3\text{B}$  precipitates, but does not continue to grow beyond  $\sim 5\%$  of the sample weight. Rather than the sharp change in the volumetric data [Fig. 1(c)] described above, the allotropic transition is reflected in Fig. 2(c) as an inflection midway through the *fcc*-Fe to *bcc*-Fe transition region labeled I. On heating, the transformation from  $\text{Fe}_{23}\text{B}_6$  to  $\text{Fe}_2\text{B}$  commences near 1050 K, accompanied by an in-

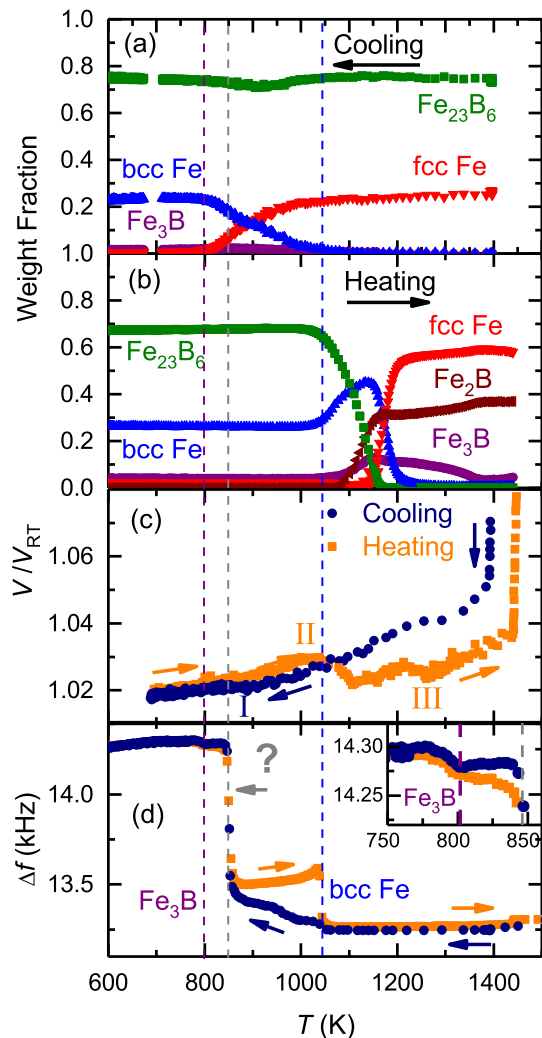


FIG. 2. (color online) (a) and (b) Results of Rietveld refinements on x-ray data. Green squares represent  $\text{Fe}_{23}\text{B}_6$ , red triangles pointing down  $fcc$  Fe, blue triangles pointing up  $bcc$  Fe, brown triangles pointing left  $\text{Fe}_2\text{B}$ , and purple circles  $\text{Fe}_3\text{B}$ . Fractions in (a) were measured on cooling, and those in (b) were measured on heating. (c) Sample volume as compared to an ambient temperature measurement. Points I through III are temperatures corresponding to transitions as described in the text. (d) The measured frequency shift in the TDO. The inset presents a detailed view of the signal near 790 K.

crease in the weight fraction of  $\text{Fe}_3\text{B}$  and  $bcc$ -Fe, consistent with the contraction in the volumetric data at point II in Fig. 2(c). The allotropic transition from  $bcc$ -Fe to  $fcc$ -Fe occurs slightly higher, between 1150 K and 1200 K in the x-ray data, and beginning at at point III near 1200K in the volume data, a discrepancy most likely due to differing heating rates between datasets. Finally, as the sample is heated above approximately 1375 K, the metastable  $\text{Fe}_3\text{B}$  transforms to  $\text{Fe}_2\text{B}$  and  $fcc$ -Fe.

Figure 2(d) displays the corresponding TDO data for this solidification pathway. In contrast to the data shown in Fig. 1(d), on cooling there is no evidence of a sharp fer-

romagnetic transition at 1040 K, consistent with the absence of the  $bcc$ -Fe at that temperature in the x-ray data. Rather, the TDO frequency shift exhibits a slow rise beginning at 1040 K, concomitant with the slow increase in the weight fraction of ferromagnetically ordered  $bcc$  Fe as temperature decreases. This can be associated with the transformation to the  $bcc$ -Fe phase. At  $T = 850$  K, there is a large increase in the TDO frequency, again indicating a transition to a ferromagnetically ordered state. There is no known  $T_C$  among the iron borides at 850 K, with the closest belonging to  $bct$ - $\text{Fe}_3\text{B}$  at 786 K and  $o$ - $\text{Fe}_3\text{B}$  at 897 K [31]. The transition at 850 K is followed by a small, reversible signal at 790 K, close to the reported  $T_C$  of  $bct$ - $\text{Fe}_3\text{B}$ , though far from the reported  $T_C$  of  $pt$ - $\text{Fe}_3\text{B}$ . This low magnitude transition, 25 Hz, could be associated with the small fraction of the sample occupied by  $\text{Fe}_3\text{B}$  (<5%). Both these signals are again present on heating, where  $bcc$  Fe shows a ferromagnetic to paramagnetic transition at 1040 K, with a magnitude reflecting the low weight fraction relative to that in the equilibrium solidification. The consistency of the  $bcc$  Fe transition at 1040 K, with a magnitude of frequency shift correspondingly related to the phase fraction of  $bcc$  Fe present, suggests that it is the only signal associated with the phase, and cannot explain the behavior observed at 850 K.

Fig. 3 corresponds to an anneal subsequent to the cooling cycle shown in Fig. 2(d). The sample was heated to  $\sim 990$  K, where the x-ray diffraction results show the beginning of a transformation from  $\text{Fe}_{23}\text{B}_6$  to  $\text{Fe}_2\text{B} + \text{Fe}_3\text{B} + bcc$  Fe, and held for eight minutes before cooling. Volume data obtained simultaneous to the TDO measurement revealed a volume contraction consistent with that seen in heating cycles similar to those present in Fig. 2. On cooling after this anneal, the frequency shift at 850 K has almost disappeared, whereas the signal at 790 K is slightly enhanced. Given the expected increase in  $\text{Fe}_3\text{B}$  content and decrease in  $\text{Fe}_{23}\text{B}_6$ , the transition at 790 K must come from  $\text{Fe}_3\text{B}$ , and the signal at 850 K can be associated with ferromagnetic ordering in  $\text{Fe}_{23}\text{B}_6$ .

#### IV. DISCUSSION AND SUMMARY

Studies have suggested that the flexibility of the  $\text{Fe}_{23}\text{B}_6$  structure allows for different fractional occupations of the Fe sites and variations in bond lengths[32], resulting in noticeable differences in the magnetic order [33]. A series of investigations by Barinov et. al [34] on single phase  $\text{Fe}_{23}\text{B}_6$  found a range of Curie temperatures from 623 K to 701 K, related to the Fe site vacancies and B concentration,  $c_B$ , of the structure by  $T_C = [101 + 26.1c_B]$  K. Nominally,  $\text{Fe}_{23}\text{B}_6$  has a  $c_B$  of 20.7%, while our recorded  $T_C$  would require a  $c_B$  of 28.7%.

Two other explanations for the higher  $T_C$  for  $\text{Fe}_{23}\text{B}_6$  seem plausible. The first, and most likely, is that this higher  $T_C$  is a result of the coherent growth of  $\text{Fe}_{23}\text{B}_6$  on large grains of metastable  $fcc$  Fe. It is unclear from

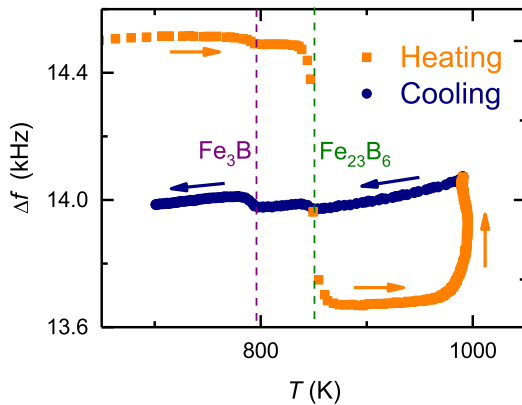


FIG. 3. (color online) TDO output from an anneal following the solidification displayed in Fig. 2(c) and (d), where the sample was heated to the temperature region where  $\text{Fe}_{23}\text{B}_6$  transforms to  $\text{Fe}_2\text{B} + bcc \text{ Fe} + \text{Fe}_3\text{B}$ . Orange squares represent the initial heat and eight minute anneal at 990 K, while blue circles represent the subsequent cool.

the Rietveld refinements and raw x-ray data if any of the *fcc* Fe remains at room temperature, and as past work has demonstrated[10], the overlap of peaks resulting from coherency together with extremely strong texturing make quantitative measurements of the *fcc* Fe and  $\text{Fe}_{23}\text{B}_6$  fractions challenging. However, the nature of the coherent stabilization might imply a kinetic barrier to further transformation at low temperature, leaving some small grains of *fcc* Fe throughout the sample.

If some *fcc* Fe is still indeed present at ambient temperatures, the possibility remains that this signal comes from stabilized *fcc* Fe clusters. There have been numerous efforts to characterize magnetic ordering in thin films of *fcc* Fe grown on Cu substrates[35] or in Cu[36] or Cu-Au[37] matrices. While *fcc* Fe is antiferromagnetic in the ground state, with a Néel temperature of 70 K[40],

metastable low-temperature *fcc* Fe growth is predicted to exhibit a sensitive dependence on its lattice parameter, varying from low-spin to high-spin ferromagnetism between 3.57 and 3.62 Å [38, 39]. The lowest temperature at which we have obtained a reliable lattice parameter of *fcc* Fe during the most recent course of work with the BESL yielded 3.628 Å at 850 K. This would imply any stabilized *fcc* Fe could be within the predicted high-spin regime.

The work performed by combination of x-ray diffraction, volume thermal expansion, and TDO susceptibility measurements paints a clear picture of magnetic transitions in the system. The equilibrium solidification displays the signature of ferromagnetic transitions in *bcc* Fe and what appears to be a primarily local moment ferromagnet,  $\text{Fe}_2\text{B}$ . Among the metastable phases, a transition at 790 K is ascribed to  $\text{Fe}_3\text{B}$ . A transition at 850 K can be safely attributed to a high Curie temperature phase resulting from  $\text{Fe}_{23}\text{B}_6$  coherently grown with *fcc* Fe. This study provides an excellent example of the capacity of containerless instrumentation to map the magnetic phase diagram of sensitive non-equilibrium phases and high-temperature materials.

#### ACKNOWLEDGMENTS

This study is based upon work supported by the National Science Foundation under Grant No. DMR-1308099. The work at Ames Laboratory was supported by the US Department of Energy, Basic Energy Sciences, of Materials Science and Engineering Division, under Contract No. DE-AC02-07CH11358. The authors wish to acknowledge the assistance of K. F. Kelton, C. Pueblo, S. Saunders, R. Ashcraft, and D.S. Robinson with the high-energy x-ray measurements, and L. Jones and M. Besser at the Materials Preparation Center at the Ames Laboratory for providing the samples in this study.

- 
- [1] J.J. Croat, J.F. Herbst, R.W. Lee, and F.E. Pinkerton, PrFe and NdFebased materials: A new class of high-performance permanent magnets, *J. Appl. Phys.*, **55** 2078 (1984).
  - [2] D. Brown, B.M. Ma, and Z. Chen, Developments in the processing and properties of NdFeB-type permanent magnets, *J. Magn. Magn. Mater.* **248**, 432, (2002).
  - [3] D. Givord, H.S. Li, and J.M. Moreau, Magnetic properties and crystal structure of  $\text{Nd}_2\text{Fe}_{14}\text{B}$  *Solid State Commun.*, **50**, 497, (1984).
  - [4] T. Kemeny, I. Vincze, B. Fogarassy, and S. Arajs, Structure and crystallization of Fe-B metallic glasses, *Phys. Rev. B* **20**, 476 (1979)
  - [5] M. Palumbo, G. Cacciamani, E. Bosco, and M. Baricco, Thermodynamic analysis of glass formation in Fe-B system, *Calphad* **25**, 625 (2002).
  - [6] L. Battezzati, C. Antonione, and M. Baricco, Undercooling of Ni-B and Fe-B alloys and their metastable phase diagrams, *J. Alloys Compd.* **247**, 164 (1997).
  - [7] C. Yang, G. Yang, F. Liu, Y. Chen, N. Liu, D. Chen, and Y. Zhou, Metastable phase formation in eutectic solidification of highly undercooled  $\text{Fe}_{83}\text{B}_{17}$  alloy melt, *Physica B* **373**, 136 (2006).
  - [8] A. Mizuno, J. Tamura, S. Kohara, and M. Watanabe, Time-Resolved X-Ray Diffraction Study on Solidification of Fe-B and Fe-C Eutectic Alloys, *Mater. Sci. Forum* **706709**, 1702 (2012).
  - [9] D. G. Quirinale, G. E. Rustan, A. Kreyssig, and A. I. Goldman, Synergistic stabilization of metastable  $\text{Fe}_{23}\text{B}_6$  and  $\gamma\text{-Fe}$  in undercooled  $\text{Fe}_{83}\text{B}_{17}$ , *Appl. Phys. Lett.* **106**, 241906 (2015).
  - [10] D. G. Quirinale, G. E. Rustan, A. Kreyssig, S Lapidus, M.J. Kramer, and A. I. Goldman, The solidification products of levitated  $\text{Fe}_{83}\text{B}_{17}$  studied by high-energy x-ray diffraction, *J. Appl. Phys.* **120**, 175104 (2016).
  - [11] E.F. Kneller and R. Hawig, The exchange-spring magnet:

- a new material principle for permanent magnets, IEEE Trans. Mag., **27**, 3588 (1991).
- [12] E.J. Escorcia-Aparicio, R.K. Kawakami, and Z.Q. Qiu, *fcc* Fe films grown on a ferromagnetic *fcc* Co (100) substrate, Phys. Rev. B, **54**, 4155 (1996).
- [13] S. Muller *et al.*, Structural instability of ferromagnetic *fcc* Fe films on Cu (100), Phys. Rev. Lett., **74**, 765 (1995).
- [14] Bagayoko, D. and Callaway, J., Lattice-parameter dependence of ferromagnetism in *bcc* and *fcc* iron, Phys. Rev. B, **28**, p.5419 (1983).
- [15] G. E. Rustan, N. S. Syrison, A. Kreyszig, R. Prozorov, and A. I. Goldman, Noncontact technique for measuring the electrical resistivity and magnetic susceptibility of electrostatically levitated materials, Rev. Sci. Instrum. **83**, 103907 (2012).
- [16] G. E. Rustan, Electrostatic levitation studies of supercooled liquids and metastable solid phases, PhD Thesis, Iowa State University, 2014
- [17] R. Prozorov, R. W. Giannetta, A. Carrington, P. Fournier, R. L. Greene, P. Guptasarma, D. G. Hinks, and A. R. Banks, Measurements of the absolute value of the penetration depth in high- $T_c$  superconductors using a low- $T_c$  superconductive coating, Appl. Phys. Lett. **77**, 4202 (2000).
- [18] J.C. Bendert, Thermophysical and Structural Measurements of Liquid Metallic Alloys using Electrostatic Levitation, PhD Thesis, Washington University, 2013
- [19] R. C. Bradshaw, D. P. Schmidt, J. R. Rogers, K. F. Kelton, and R. W. Hyers, Machine vision for high-precision volume measurement applied to levitated containerless material processing, Rev. Sci. Instrum., **76**, 125108, (2005).
- [20] N. A. Mauro and K. F. Kelton, A highly modular beamline electrostatic levitation facility, optimized for in situ high-energy x-ray scattering studies of equilibrium and supercooled liquids, Rev. Sci. Instrum. **82**, 035114 (2011).
- [21] C.A. Schneider, W.S. Rasband, and K.W. Eliceiri, NIH Image to ImageJ: 25 years of image analysis, Nature Methods **9**, 671 (2012)
- [22] A. P. Hammersley, ESRF Internal Report, ESRF97HA02T, "FIT2D: An Introduction and Overview", Grenoble, France (1997)
- [23] A. P. Hammersley, S O Svensson, and A Thompson, Calibration and correction of spatial distortions in 2D detector systems, Nucl. Instr. Meth., **A346**, 312, (1994)
- [24] A. C. Larson and R. B. Von Dreele, Technical Report LAUR 86-748, Los Alamos National Laboratory, Los Alamos, USA (2004).
- [25] K.A. Murphy and N. Hershkowitz, Temperature-dependent hyperfine interactions in Fe<sub>2</sub>B, Phys. Rev. B, **7**, 23 (1973).
- [26] M.D. Vannette *et al.*, Precise measurements of radio-frequency magnetic susceptibility in ferromagnetic and antiferromagnetic materials, J. Magn. Magn. Mater. **320** 354 (2008)
- [27] M. D. Vannette, Dynamic magnetic susceptibility of systems with long-range magnetic order, PhD Thesis, Iowa State University, 2009
- [28] P.J. Brown and J.L. Cox, Charge and spin density distributions in the ferromagnetic alloy Fe<sub>2</sub>B, Phil. Mag. **23**, 705 (1971).
- [29] T.B. Massalski and D.E. Laughlin, The surprising role of magnetism on the phase stability of Fe (Ferro), Calphad, **33**, 3-7 2009.
- [30] Schenk, T., Holland-Moritz, D. and Herlach, D.M., Observation of magnetically induced crystallization of undercooled Co-Pd alloys, Europ. Phys. Lett., **50**, 402, (2000).
- [31] D. Fruchart, P. Chaudouet, R. Fruchart, A. Rouault, and J. P.Senateur, Etudes structurales de composés de type cémentite: Effet de l'hydrogène sur Fe<sub>3</sub>C suivi par diffraction neutronique. Spectrométrie Mössbauer sur FeCo<sub>2</sub>B et Co<sub>3</sub>B dopés au <sup>57</sup>Fe, J. Solid State Chem. **54**, 246 (1984)
- [32] V.A. Barinov and V.T. Surikov., Short-range atomic order in the metastable Fe<sub>23</sub>B<sub>6</sub> phase Phys. Met. Metallogr **105**, 262 (2008)
- [33] C.M. Fang, M.A. Van Huis, M.H.F. Sluiter, and H.W. Zandbergen, Stability, structure and electronic properties of  $\gamma$ -Fe<sub>23</sub>C<sub>6</sub> from first-principles theory, Acta Mater. **58**, 2968 (2010).
- [34] V.A. Barinov, V.A. Tsurin, V.I. Voronin, S.I. Novikov, and V.T. Surikov, Mössbauer investigations of the metastable Fe<sub>23</sub>B<sub>6</sub> phase, Phys. Met. Metallogr. **101**, 456 (2006).
- [35] C. A. F. Vaz, J. A. C. Bland, and G. Lauhoff, Magnetism in ultrathin film structures, Rep. Prog. Phys. **71**, 056501 (2008), and references therein.
- [36] Y. Tsunoda, S. Imada, and N. Kunitomi, Anomalous lattice contraction and magnetism of  $\gamma$ -Fe precipitates in Cu, J. Phys. F: Met. Phys. **18**, 1421(1988).
- [37] U. Gonser, K. Krischel, and S. Nasu, Ferromagnetic ordering in *fcc*  $\gamma$ -Fe precipitates in Cu-Au alloys, J. Magn. Magn. Mater. **15**, 1145 (1980).
- [38] L. T. Kong, and B. X. Liu, Correlation of magnetic moment versus spacing distance of metastable *fcc* structured iron, App. Phys. Let. **84**, 3627 (2004)
- [39] L. T. Kong and B. X. Liu, Distinct magnetic states of metastable *fcc* structured Fe and FeCu alloys studied by ab initio calculations, J. Alloys Compd. **414**, 36 (2006)
- [40] S. C. Abrahams, L. Cuttman, and J. S. Kasper, Neutron diffraction determination of antiferromagnetism in face-centered cubic ( $\gamma$ ) iron, Phys. Rev. **127**, 2052 (1962).